DETERMINING THE NATURE OF THE SS 433 BINARY FROM AN X-RAY SPECTRUM DURING ECLIPSE

Laura A. Lopez,[1,2,3] Herman L. Marshall,[4] Claude R. Canizares,[4] Norbert S. Schulz,[4] and Julie F. Kane[3,5]

ABSTRACT

We test the physical model of the relativistic jets in the Galactic X-ray binary SS 433 proposed in our previous paper using additional observations from the *Chandra* High Energy Transmission Grating Spectrometer. These observations sample two new orbital/precessional phase combinations. In the observation near orbital phase zero, the H- and He-like Fe lines from both receding and approaching jets are comparably strong and unocculted while the He-like Si line of the receding jet is significantly weaker than that of the approaching jet. This condition may imply that the cooler parts of the receding jet are eclipsed by the companion. The X-ray spectrum from this observation has broader emission lines than obtained in Paper I that may arise from the divergence of a conical outflow or from Doppler shift variations during the observation. Using recent optical results, along with the length of the unobscured portion of the receding jet assuming adiabatic cooling, we calculate the radius of the companion to be $9.6 \pm 1.0\ R_\odot$, about one-third of the Roche lobe radius. For a main-sequence star, this corresponds to a companion mass of $35 \pm 7\ M_\odot$, giving a primary source mass of $20 \pm 5\ M_\odot$. If our model is correct, this calculation indicates that the compact object is a black hole, and accretion occurs through a wind process. In a subsequent paper, we will examine the validity of the adiabatic cooling model of the jets and test the mode of line broadening.

Subject headings: X-rays: binaries — X-rays: individual (SS 433)

1. INTRODUCTION

The Galactic X-ray binary SS 433 is the only known astrophysical jet system in which relativistically red- and blueshifted lines are observed from high-Z elements. Lines from the H Balmer series were detected (Margon et al. 1979) and modeled kinematically (Abell & Margon 1979; Fabian & Rees 1979; Milgrom 1979) as emission from opposing jets emerging from the vicinity of a compact object that precesses about an axis inclined to the line of sight. The jet velocity v_j is $0.260c$, and its orientation precesses with a 162.5 day period in a cone with half-angle $19°.85$ about an axis that is $78°.83$ to the line of sight (Margon & Anderson 1989). The lines from the jet are Doppler shifted with this period so that the maximum redshift is about 0.15 and the maximum blueshift is about -0.08. The X-ray source undergoes eclipses at a 13.0820 day period. Assuming uniform outflow, the opening angle of the jet is $5°$ based on the widths of the optical lines (Begelman et al. 1980). For more details of the optical spectroscopy, see the review by Margon (1984).

SS 433 has radio jets oriented at a position angle of $100°$ (east of north) that show an oscillatory pattern that arises from helical motion of material flowing along ballistic trajectories (Hjellming & Johnston 1981). Using VLBI observations of ejected knots, Vermeulen et al. (1993) independently confirmed the velocity of the jet and the kinematic model and also derived an accurate distance: 4.85 ± 0.2 kpc. We adopt this distance throughout our analysis. The radio jets extend from the milliarcsecond scale to several

arcseconds, a physical range of 10^{15}–10^{17} cm from the core. The optical emission lines, however, originate from a smaller region, $<3 \times 10^{15}$ cm across, based on light-travel time arguments (Davidson & McCray 1980).

Using *HEAO-1* (*High Energy Astronomical Observatory*), Marshall et al. (1979) were the first to demonstrate that SS 433 is an X-ray source. The *HEAO-1* continuum was sufficiently modeled as thermal bremsstrahlung with $kT = 14.3$ keV, and emission due to Fe K was detected near 7 keV. Based on *Ginga* observations, Brinkmann et al. (1991) concluded that kT is $\approx$30 keV, while Kotani et al. (1996) obtained a value of 20 keV based on the ratio of Fe xxv and Fe xxvi line fluxes from the *Advanced Satellite for Cosmology and Astrophysics* (*ASCA*). The X-ray emission may originate from the base of the jets, which adiabatically expand and cool until kT drops to $\approx$100 eV and become thermally unstable (Brinkmann et al. 1991; Kotani et al. 1996). Kotani et al. (1996) found that the redshifted Fe xxv line was fainter relative to the blueshifted line than expected from Doppler intensity conservation. Consequently, they concluded that the redward jet must be obscured by neutral material in an accretion disk. Although the *ASCA* spectra showed emission lines that were previously unobserved, the lines were not resolved spectrally and lines below 2 keV were difficult to identify.

Marshall et al. (2002, hereafter Paper I) observed SS 433 with the High Energy Transmission Grating Spectrometer (HETGS; Canizares et al. 2005) of the *Chandra X-Ray Observatory*. This observation resolved the X-ray lines, detected fainter lines than previously observed, and measured lower energy lines than could be readily detected in the *ASCA* observations. In addition, the HETGS spectrum of SS 433 showed many emission lines previously identified in the *ASCA* observations (Kotani et al. 1994). In Paper I, the X-ray spectrum was dominated by thermal emission from the jets. In addition, using the Si xiii triplet, the electron density of the jet was determined to be 10^{14} cm^3, facilitating an estimate for the size of the jet, $(2-20) \times 10^{10}$ cm.

In Paper I, blueshifted lines dominated the spectrum and the redshifted lines were all relatively weak by comparison, so most

[1] Department of Astronomy and Astrophysics, University of California, Santa Cruz, 355 Interdisciplinary Sciences Building, 1156 High Street, Santa Cruz, CA 95064; lopez@astro.ucsc.edu.

[2] Institute for Advanced Study, School of Natural Sciences, Einstein Lane, Princeton, NJ 08540.

[3] NSF Graduate Research Fellow.

[4] Department of Physics and Kavli Institute for Astrophysics and Space Research, Massachusetts Institute of Technology, Cambridge, MA 02139; hermanm@space.mit.edu, crc@space.mit.edu, nss@space.mit.edu.

[5] Department of Earth, Atmospheric, and Planetary Science, Massachusetts Institute of Technology, Cambridge, MA 02139; jfkane@mit.edu.
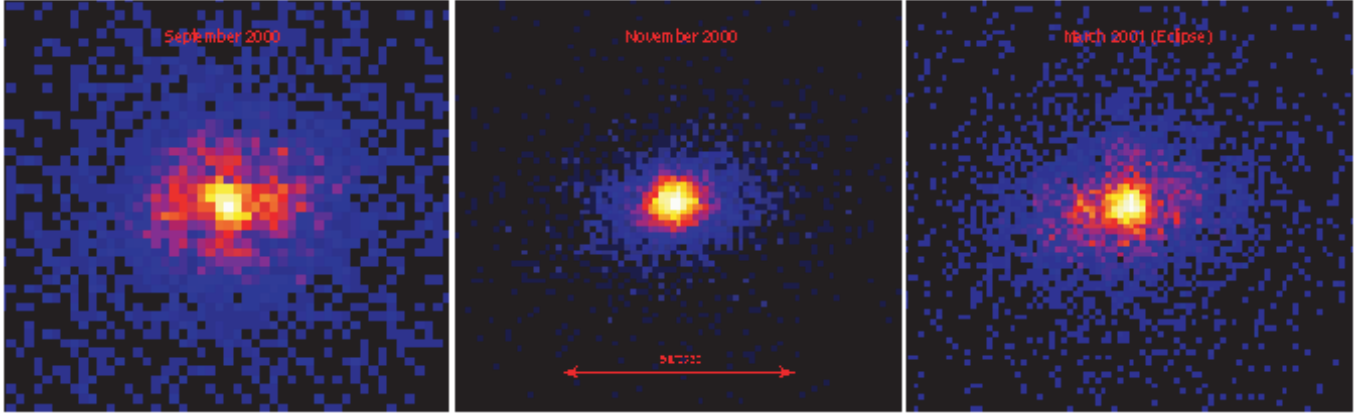
Fig. 1.—Images of SS 433 from the zeroth order of the *Chandra* HETGS. The images are extended along the east-west direction on a scale of $2''$–$5''$ as discovered by Marshall et al. (2002 [Paper I]). The extent is comparable to that observed in the radio band by Hjellming & Johnston (1981). The left image was taken when the eastern jet neared maximal blueshift (Paper I). In the second observation (*middle*), the jet precessed around to point away from the observer, making it more redshifted than the western jet. Finally, the 2001 March observation was taken at the same precessional phase as the first image, but the source was eclipsed. Possible north-south structure in the first observation was not confirmed in later images. The point source was weakest in 2000 November. Note that the point source is still very bright during eclipse, indicating that the innermost, hottest regions of the jets are not occulted.

work focused on modeling the blue jet. The jet velocity was determined very accurately due to the small scatter of individual line Doppler shifts and the narrowness of their profiles, indicating that all line-emitting gas flows at the same speed. The jet bulk velocity was βc, where $\beta = 0.2699 \pm 0.0007$. This jet velocity is larger than the model velocity inferred from optical emission lines by 2920 ± 440 km s^{-1}. Gaussian fits to the emission lines were all consistent with the same Doppler broadening: 1700 ± 80 km s^{-1} (*FWHM*). Relating this broadening to the maximum velocity due to beam divergence, the opening angle of the jet was determined to be $1°23 \pm 0°06$.

Here we present new observations of SS 433 using the HETGS to test the physical model of the jets proposed in Paper I. The new observations were taken at two different combinations of precessional and orbital phases, offering contrasting views of the jets. In particular, one observation was taken during eclipse. The goal of the observation was to determine which parts of the jets would be occulted due to this eclipse. The results of the optical observations presented by Gies et al. (2002a), along with the length of the jets determined assuming an adiabatic cooling model, are utilized to measure the size and mass of the companion. This analysis will set a restriction on the mass of the compact object and ultimately support the hypothesis that the primary source is a black hole. Our conclusions rely on the postulate that adiabatic cooling dominates over radiative losses, and we discuss the limitations of this model in § 5.1.

Previous X-ray observations of the SS 433 system during eclipse (Brinkmann et al. 1991; Stewart et al. 1987) also displayed weak emission lines from the receding jet. This result has led some to believe that the entire inner region of the jets was eclipsed. However, our spectrum during occultation shows numerous emission lines from the receding jet. Particularly, the presence of strong, highly ionized Fe lines indicates that only the low-energy portion of this jet was eclipsed.

2. OBSERVATIONS AND DATA REDUCTION

SS 433 was observed with the HETGS on 2000 November 21 and 2001 March 16 for 24 ks each, observation IDs 1020 and 1019. The latter observation was taken during eclipse when the companion blocked part of the X-ray continuum. Based on the precession ephemeris by Margon & Anderson (1989) as updated

by Gies et al. (2002b), the angle of the jet to the line of sight during this observation was predicted to be $\alpha = 80°0$. From the precession and binary ephemeris by Gladyshev et al. (1987), the binary phase range was 0.96–0.98. For observation 1020, α was $96°0$ (meaning that the normally approaching western jet was temporarily pointed farther from the line of sight than the normally receding eastern jet) and the binary phase range was 0.68–0.70.

2.1. *Imaging*

The zeroth-order image from the three observations (the Paper I observation and the two presented in this paper) is shown in Figure 1 and is distinctly elongated in the east-west direction. The extended X-ray emission was first reported in Paper I. This result is consistent with Fender et al. (2003), who found evidence for outflowing hot plasma in the extended X-ray emission. The scale of emission is 10^4 times larger than the region producing the bulk of the X-ray spectrum, indicating that plasma is reheating very far from the compact object. The excess emission in the east-west direction is associated with the arcsecond-scale radio jet, as observed by Hjellming & Johnston (1981) using the Very Large Array. Based on the dispersed spectra (because the point source is somewhat piled up, as in Paper I), the X-ray flux from SS 433 was constant during observation 1019 but increased by about 15% on a timescale of 10,000 s in 2000 November.

2.2. *Spectra*

As in Paper I, the spectral data were reduced starting from level 1 data provided by the Chandra X-Ray Center (CXC) using IDL custom processing scripts. The spectra from the 2001 March and 2000 November observations are shown in Figures 2 and 3, respectively. The jet emission lines are much weaker in the 2000 November observation than in 2001 March or Paper I. Consequently, the 2000 November observation is not analyzed further in this paper, and we only discuss results from 2001 March as compared to Paper I.

Line fluxes for the 2001 March observation are given in Table 1. A methodology similar to that of the first paper was utilized: lines were fit to the MEG and HEG data jointly in five wavelength ranges after subtracting a polynomial fit to the continuum. Gaussian widths are given in Table 2. Only statistical errors are
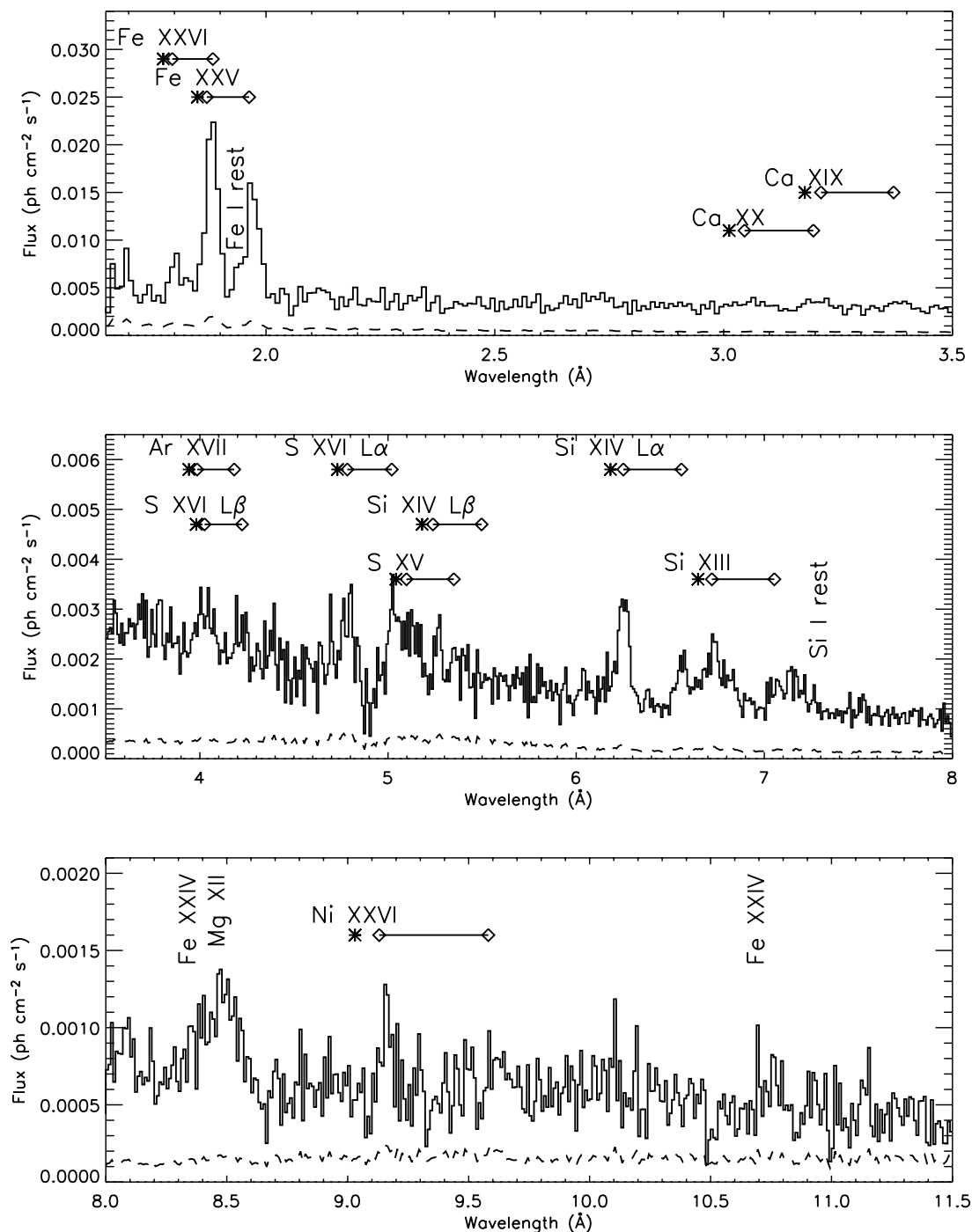
Fig. 2.—X-ray spectrum of SS 433 observed with *Chandra* HETGS in 2001 March. The HEG and MEG data were combined at the resolution of the MEG spectrum. Line identifications are shown, and measurements are given in Table 1. Horizontal lines connect the locations of blue- and redshifted lines (*diamonds*) to the rest wavelengths (*asterisks*). The dashed line gives the statistical uncertainties. Emission lines are resolved, and their strengths indicate that the plasma is collisionally dominated. The Fe xxv line from the approaching jet is confused with the Fe xxvi line of the receding jet.

quoted; systematic uncertainties other than possible line mis-identifications are expected to be smaller than 10%. The lines are twice as broad as those found in the first observation. The spectra are shown in Figures 2–6. Figure 2 shows the flux-corrected spectrum, combining the MEG and HEG data with statistical weighting. Similar to the first observation, many broad emission lines and a significant continuum are prevalent. Unlike Paper I, where some red jet lines were undetectably weak, every blue jet line has a corresponding red jet line in the 2001 March observation.

For each line, the ID was determined based on the expected shifts of the blue and red jets from the kinematic model and the measured redshift. For the precession phase of our observation, the predicted blue- and redshifts were 0.011 and 0.063, respectively, using the equation and parameters in Table 1 of Margon & Anderson (1989). Wavelengths of line blends were obtained using wavelengths from the Astrophysical Plasma Emission Database (APED)[6]

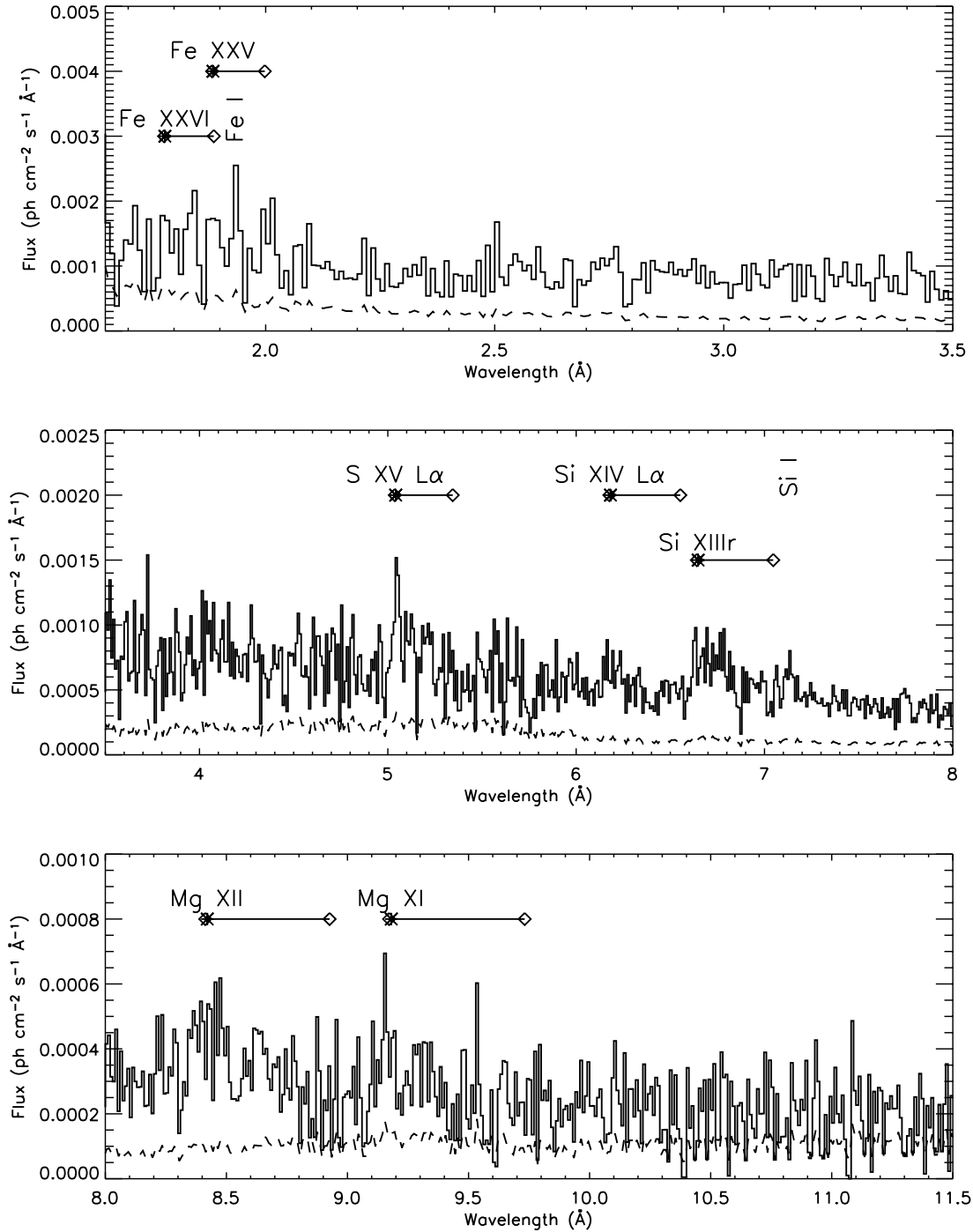[6] See http://cxc.harvard.edu/atomdb/sources_aped.html for more information about APED.

FIG. 3.—X-ray spectrum of SS 433 observed with *Chandra* HETGS in 2000 November, shown as in Fig. 2. Possible line identifications are shown. Lines were extremely weak during this observation in both the red jet ($z_r = 0.070$) and blue jet ($z_b = -0.001$). The overall flux level is very low compared to the observation reported in Paper I and the 2001 March observation (Fig. 2).

weighted by the relative fluxes of each component based on the models from § 5. The S xv and Si xiii triplets were analyzed as in Paper I. Precise redshifts for these profiles were determined by fitting these blends with several variable width Gaussian components and with fixed rest wavelength values given by APED, as implemented in the Interactive Spectral Interpretation System (ISIS).[7] Unlike in Paper I, the red and blue jet lines were

prominent enough to facilitate accurate measurement of the redshift for both jets. Two lines were assigned to neither the red nor the blue jets: a neutral Fe K line and a Si i K line, both at rest in the observed frame.

3. LINE WIDTHS AND POSITIONS

Table 1 shows that the Doppler shifts of the lines in the blue jet system are consistent with a single velocity to within the uncertainties, as are those in the red jet system. The few deviations are

[7] See http://space.mit.edu/CXC/ISIS for more information about ISIS.

TABLE 1
SS 433 X-Ray Emission Lines

$\lambda_{\rm rest}$ (Å)	$\lambda_{\rm obs}$ (Å)	z	Flux (10^{-6} photons cm^{-2} s^{-1})	Identification
		Blue Jet		
1.780	1.804 ± 0.004	0.0133 ± 0.0020	116 ± 25	Fe xxvi Lyα
1.855	1.881 ± 0.009	0.0144 ± 0.0049	593 ± 37	Fe xxv $1s2p-1s^2$ [a]
3.020	3.061 ± 0.009	0.0136 ± 0.0029	33 ± 10	Ca xx Lyα
3.186	3.207 ± 0.007	0.0066 ± 0.0021	46 ± 10	Ca xix $1s2p-1s^2$ [b]
3.952	4.004 ± 0.007	0.0130 ± 0.0016	31 ± 10	Ar xvii $1s2p-1s^2$
3.991	4.047 ± 0.005	0.0140 ± 0.0014	105 ± 16	S xvi Lyβ
4.729	4.788 ± 0.005	0.0124 ± 0.0010	88 ± 14	S xvi Lyα
5.055	5.128 ± 0.006	0.0143 ± 0.0012	88 ± 13	S xv $1s2p-1s^2$
5.217	5.262 ± 0.007	0.0085 ± 0.0013	53 ± 12	Si xiv Lyβ
6.141	6.249 ± 0.002	0.0108 ± 0.0003	142 ± 8	Si xiv Lyα
6.675	6.730 ± 0.003	0.0083 ± 0.0004	88 ± 7	Si xiii $1s2p-1s^2$
8.310	8.379 ± 0.011	0.0083 ± 0.0014	22 ± 5	Fe xxiii/xxiv
8.421	8.493 ± 0.005	0.0085 ± 0.0006	61 ± 6	Mg xii Lyα [c]
9.103	9.166 ± 0.010	0.0071 ± 0.0011	25 ± 7	Ni xxvi
10.636	10.742 ± 0.013	0.0100 ± 0.0012	31 ± 6	Fe xxiv
		Rest Frame		
1.937	1.942 ± 0.004	0.0025 ± 0.0018	100 ± 21	Fe i
7.128	7.131 ± 0.006	0.0004 ± 0.0008	14 ± 3	Si i–Si vii
		Red Jet		
1.780	1.881 ± 0.001	0.0570 ± 0.0005	593 ± 37	Fe xxvi Lyα [a]
1.855	1.973 ± 0.001	0.0641 ± 0.0006	348 ± 28	Fe xxv $1s2p-1s^2$
3.020	3.207 ± 0.007	0.0619 ± 0.0022	46 ± 10	Ca xx Lyα [b]
3.186	3.382 ± 0.007	0.0614 ± 0.0021	41 ± 10	Ca xix $1s2p-1s^2$
3.952	4.213 ± 0.008	0.0659 ± 0.0020	57 ± 11	Ar xvii $1s2p-1s^2$
3.991	4.213 ± 0.008	0.0557 ± 0.0020	57 ± 11	S xvi Lyβ
4.729	5.033 ± 0.004	0.0643 ± 0.0008	113 ± 13	S xvi Lyα
5.055	5.354 ± 0.013	0.0591 ± 0.0026	37 ± 12	S xv $1s2p-1s^2$
6.182	6.561 ± 0.004	0.0612 ± 0.0006	58 ± 6	Si xiv Lyα
6.675	7.057 ± 0.006	0.0573 ± 0.0010	32 ± 5	Si xiii $1s2p-1s^2$
7.989	8.493 ± 0.005	0.0630 ± 0.0007	61 ± 6	Fe xxiv [c]
9.103	9.637 ± 0.013	0.0588 ± 0.0014	25 ± 6	Ni xxvi

[a] The red jet Fe xxvi Lyα line is blended with the blue jet Fe xxv line.
[b] The red jet Ca xx Lyα line is blended with the blue jet Ca xix line.
[c] The red jet Fe xxiv line is blended with the blue Mg xii Lyα line.

mostly due to blended lines (e.g., line triplets) in each jet and are not likely indicative of intrinsic variations. Furthermore, all deviations are substantially smaller than the observed line widths, which are on the order of $\delta z = 0.006$. The Doppler shift of the blue jet was determined to be $z_b = 0.0111 \pm 0.0001$ during this observation (as opposed to the $z_b = -0.0779 \pm 0.0001$ in Paper I). For the red jet, the unblended lines give $z_r = 0.0610 \pm$

TABLE 2
Line Widths

Wavelength Range (Å)	v [a] (km s^{-1})
1.5–2.5	1500 ± 100
2.5–4.0	1600 ± 350
4.0–5.5	1600 ± 200
5.5–7.5	1200 ± 50
7.5–11.5	1200 ± 100

[a] Velocity width (σ) of Gaussian line profiles.

0.0001 (compared to the $z_r = 0.1550 \pm 0.0004$ reported in Paper I).

As in Paper I, we assume that the system is comprised of two perfectly opposed jets at an angle α to the line of sight. Then, the Doppler shifts of the blue and red jets are given by

$$z = \gamma(1 \pm \beta\mu) - 1, \qquad (1)$$

where $v_j = \beta c$ is the velocity of the jet flow, $\gamma = (1 - \beta^2)^{-1/2}$, and $\mu = \cos\alpha$. As in the first paper, high-accuracy redshifts were used to obtain an estimate of the γ and β by adding the Doppler shifts to cancel the $\beta\mu$ terms:

$$\gamma = \frac{z_b + z_r}{2} + 1, \qquad (2)$$

giving $\beta = 0.2666 \pm 0.0006$. This value is slightly smaller than the β obtained in the first paper, 0.2699 ± 0.0007, and is closer to, but still larger than, the jet velocity determined by Margon & Anderson (1989) based on the Hα lines. Substituting the value for

TABLE 3
Jet Parameters from a Multitemperature Model

Zone	T (10^6 K)	Blue Jet EM (10^{57} cm^3)	Red Jet EM (10^{57} cm^3)	r (10^{10} cm)	n_e (10^{14} cm^{-3})
1................	6.3	4.72	0	20.5	0.40
2................	12.6	4.60	0	12.2	1.00
3................	31.6	8.63	8.63	6.13	4.00
4................	126	8.83	8.83	2.17	20.0

Notes.—The interstellar absorption column density was fit simultaneously with the EM values at each temperature. The best-fit absorption column was fixed at 2.07×10^{22} cm^{-2}. The values of r and n_e are derived using the adiabatically expanding jet model determined in Paper I.

β back into equation (1) and solving for α gives the angle of the jet to the line of sight during this observation: $\alpha = 84°.6 \pm 0°.1$.

All jet lines are clearly resolved. The line widths in Table 2 are consistent with the weighted average value (σ) of 1430 ± 167 km s^{-1}. We note that σ is ≈ 2 times the value in Paper I: the observed lines are twice as broad as those reported in Paper I. Marginal evidence exists indicating a trend that the lower energy lines are slightly narrower than average. As found in Paper I, the widths of the red jet lines are consistent with those of the blue jet.

The line widths are too large to result from thermal broadening for $kT < 10$ keV (see § 4): 100–200 km s^{-1}. The Doppler-broadened widths may result from the divergence of a conical outflow (Begelman et al. 1980) or from Doppler shift variations during the observation. We will investigate the relationship between broadening and Doppler shift variations in a subsequent

paper on a recent HETGS observation of SS 433 (Marshall et al. 2006). The origin of the line broadening does not affect the line flux measurements and the plasma modeling of the next section.

4. THE JET EMISSION-LINE FLUXES

To model the X-ray spectra, we use a plasma diagnostic approach where emission lines correspond to specific jet temperatures. In both the red and blue jets, we observe comparable line strengths in Fe, Ca, and Ar. Longward of 4 Å the red jet lines become weaker than the blue jet lines. We assume that this effect arises from occultation of the low-energy part of the red jet by the companion star. Although Si and S are present in the red jet, these lines are not as strong as expected given the blue jet line fluxes. Therefore, we model the red jet with comparatively lower emission measures at longer wavelengths.

As in Paper I, the spectra were modeled using ISIS and the APED atomic database of line emissivities and ionization balance. The emission measure distribution was estimated by fitting the line flux data to a multitemperature emission model assuming approximately solar abundances. Starting from the model used to analyze the first observation, a moderately good fit was obtained to the line fluxes with a four-component model for both jets, as given in Table 3. We assumed that the ISM absorption was the same as determined in Paper I: $N_H = (2.07 \pm 0.07) \times 10^{22}$ cm^{-2}. See Figures 4, 5, and 6 for a detailed comparison of the models with the HETGS data. No formal uncertainties are given for the values in Table 3, but by comparison to the analysis (Table 4 of Paper I), we estimate the uncertainties to be $\pm 30\%$.
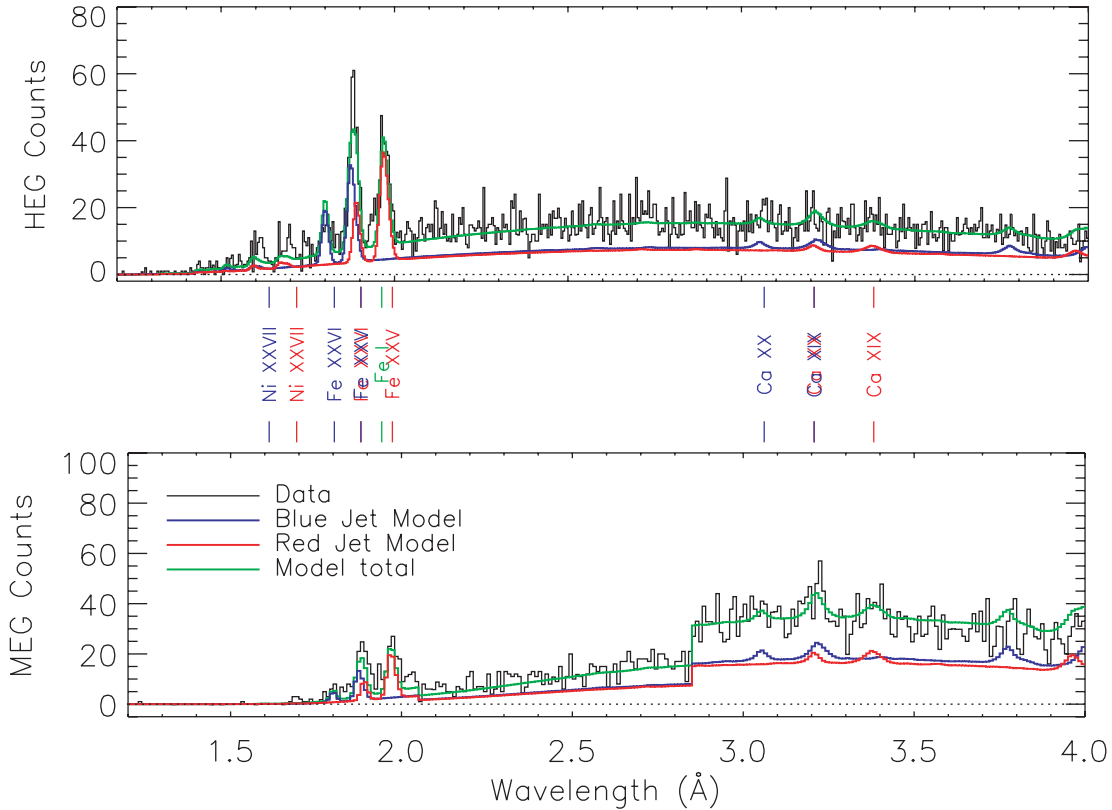

Fig. 4.—The 1.2–4.0 Å portions of the HEG and MEG spectra of SS 433 observed with *Chandra* HETGS, compared to models of the spectra of the blue and red jets. The sum of the red and the blue spectra give the green curve. Line identifications are shown, and measurements are given in Table 1. The continuum is dominated by thermal bremsstrahlung emission. The edge in the spectrum at 2.8 Å is the result of excising data near a detector chip gap. In comparison to the first observation, the emission lines are more redshifted. The Fe I line, at rest in the observed frame, is in the same location. The blue and red jet Fe xxv and Fe xxvi lines are of nearly equal strength in the model, indicating that the hottest portions of the jets are not blocked by the companion during eclipse.
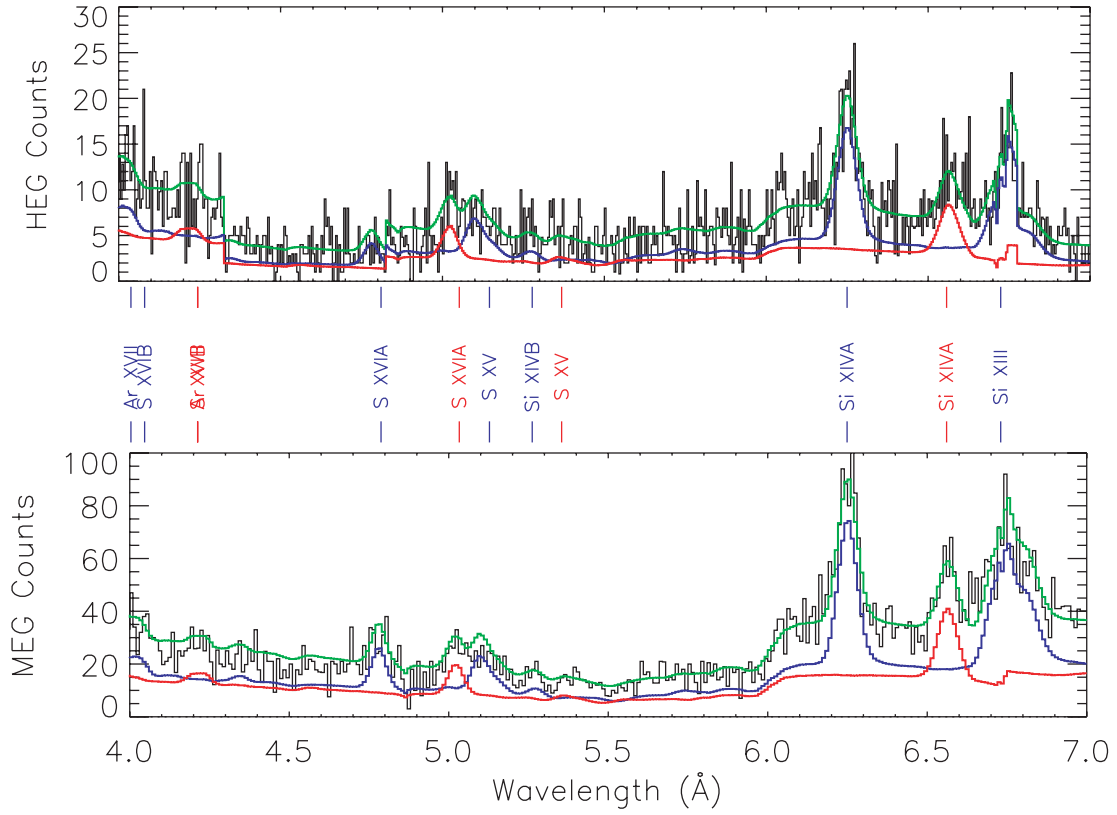
FIG. 5.—Same as Fig. 4, but for the 4.0–7.0 Å region. Unlike the first observation, the red jet is still strong in this portion of the spectrum. The overall model continuum is slightly higher than the data in the 4–6 Å range, but the Si XIV and Si XIII lines are well fit. Because the model includes the instrumental response, there is a steep rise near 6.1 Å that results from the mirror Ir-M edge.
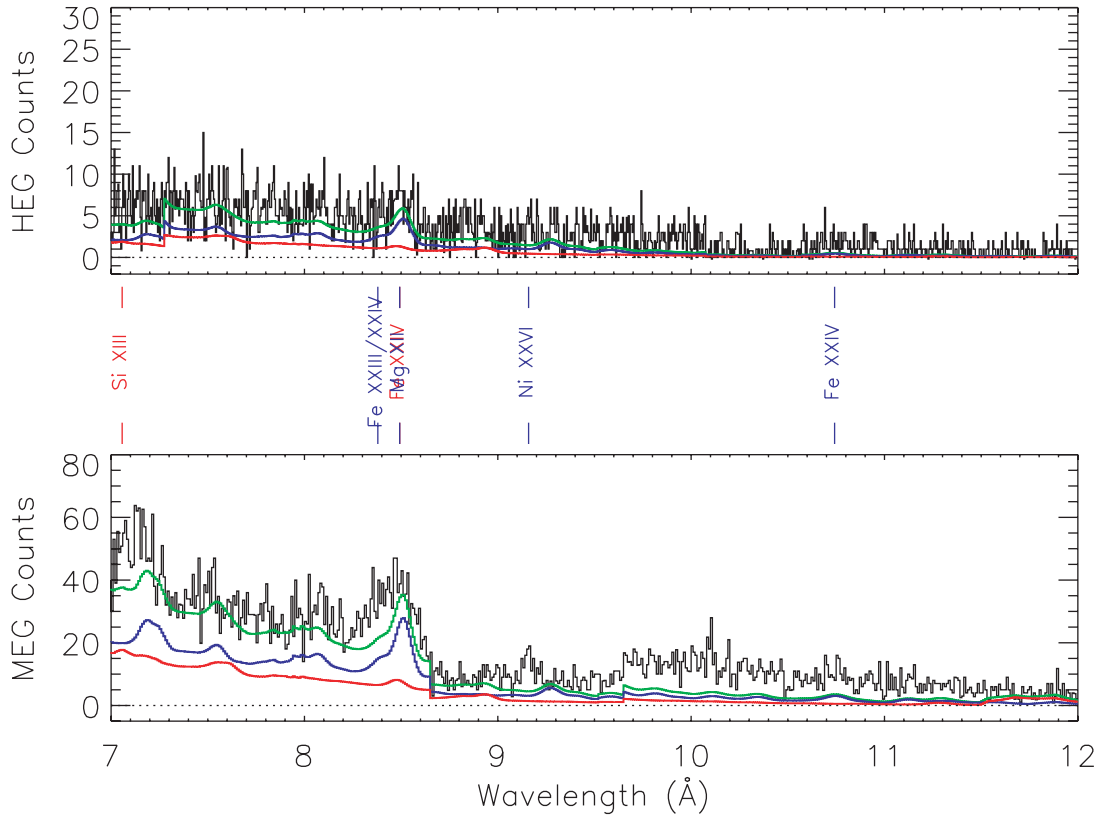

FIG. 6.—Same as Fig. 4, but for the 7.0–12.0 Å region. As in Paper I, the overall model continuum is lower than the data in this wavelength range. In addition, fewer emission features can be distinguished. There is excess emission near the red Si XIII line, which can be attributed to a Si I fluorescence line that is not included in the plasma model.
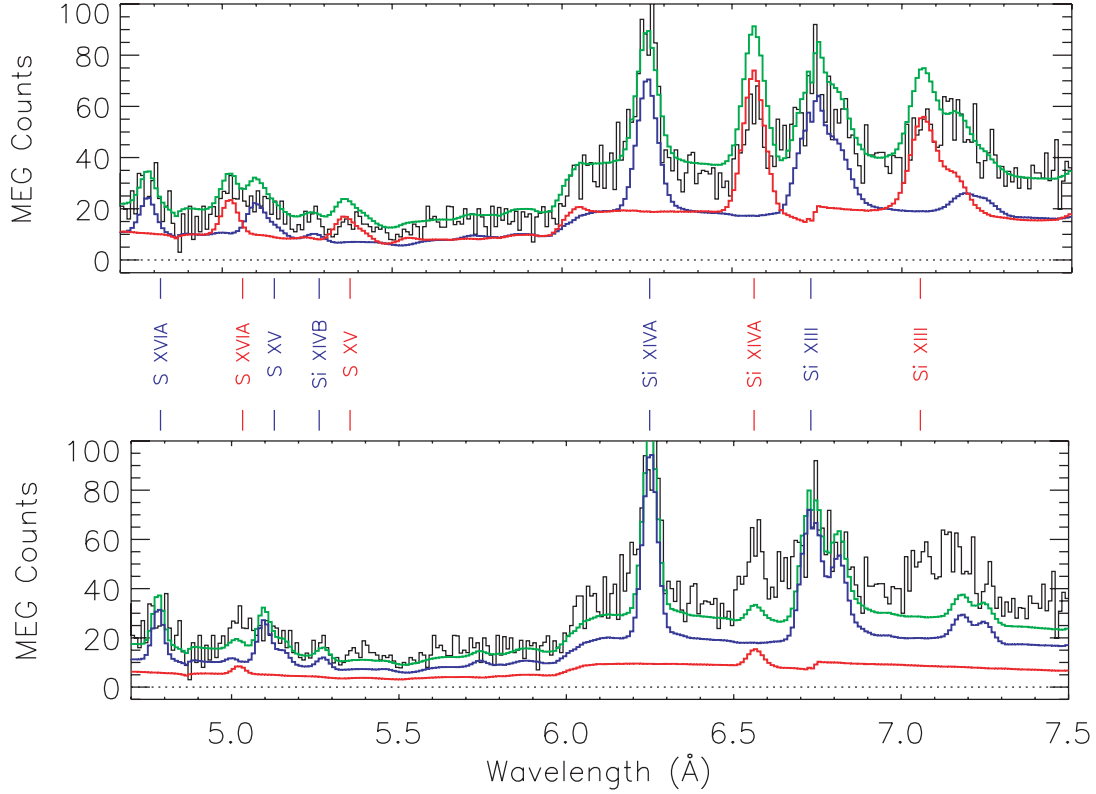
Fig. 7.—Examples of poor fits obtained by varying the emission measures of zones 2 and 3 (see Table 3) in the red jet model. The models are color coded as in Fig. 4. *Top:* Spectra and models using the same emission measures for zones 2 and 3 in the red jet model as in the blue jet model. The S xv, Si xiv, and Si xiii lines in the red jet are significantly overpredicted. *Bottom:* Same, but with second and third emission measures set to zero in the red jet model. In this case, the S xv, Si xiv, and Si xiii lines are almost nonexistent in the red jet model.

The abundances of Fe, S, Si, Mg, and Ne in the models for both jets were increased by 70% relative to H and He in order to reduce the model continuum to match the observed continuum. In Paper I, the abundances were increased 30% over the solar values. The continuum fits well over much of the spectrum, but in the 8–12 Å region, the model predicts a continuum that is systematically low by up to a factor of 2. Adding a fifth, low-temperature component, however, predicted emission lines that are not observed.

For the red jet, the same four-temperature model was used as for the blue jet. The two low-temperature components were set to zero to model the low-energy portion of the red jet as blocked by the companion due to eclipse. The resulting two-temperature model is given in Table 3. This method produced reasonable agreement with the data except around the red jet Si xiii line.

Given the broader emission lines in the 2001 March observation, the lack of Doppler boosting, and the slightly shorter exposure time compared to the Paper I observation, the analysis of the Si xiii triplet did not produce stringent limits on the jet electron density. In the blue jet, the value of the ratio of the forbidden and intercombination lines, $R \equiv f/i = 1.79 \pm 0.70$, is consistent with the value determined in Paper I. However, it is also consistent with the asymptotic value as n_e drops below 10^{12} cm^{-3} for a plasma with $T = 5 \times 10^7$ K (where Si xiii is formed). We note that the blue jet Si xiii triplet was better resolved in the Paper I observation, and the Paper I measured R-value corresponded to $n_e \approx 10^{14}$ cm^{-3}. This electron density is consistent with the assumption that flow time is much greater than the recombination timescale. The Si i fluorescence line is confused somewhat with the Si xiii of the red jet, making it difficult to compare its R- or G-values with those of the blue jet.

The spectrum is more complex than the model suggests: additional lines may be present at 8.1 and 10.1 Å that are not included in the model, and the line at 5.1 Å (S xv in the blue jet) appears to be slightly stronger in the model than in the data. The Si xiii red jet line and the Fe xxiii/xxiv blue jet line are much stronger than the model's prediction. We note that Fe xxiii/xxiv is not detected from the red jet due to eclipse, and the blue jet Fe xxiii/xxiv discrepancy may arise from deviation from ionization equilibrium at low temperatures in both jets. Almost all the other line fluxes are matched to within 50%, and the strongest lines are modeled to within 10%–20%. We consider the overall fit to be reasonably satisfactory.

It is clear from Figure 4 that the highly ionized Fe lines are not occulted during the eclipse, whereas lower ionization states of Si are not as strong in the receding jet (Fig. 5) as in the approaching jet. Thus, we interpret this result as indicating that the cooler part of the red jet is blocked by the companion, whereas the hotter portions (where the Fe lines are produced) are unocculted. We assume that the jet flow is conical and has a constant opening angle and jet velocity (as in Fig. 9 of Paper I) because ions in different temperature ranges have similar line widths and Doppler shifts. Consequently, the electron density n_e is proportional to r^{-2}, where r is the distance from the apex of the cone.

Approximate values for the plasma parameters were determined iteratively in about 50 runs of the ISIS four-zone model. Once we found a satisfactory model for the blue jet (see Table 3), the next step was to distinguish the physical differences in the red jet. To calculate the range of acceptable emission measures for the red jet in the four-zone model, we varied the emission measures in zones 2 and 3, while the zone 1 emission measure was set to zero and the zone 4 emission measure was set equal to the value
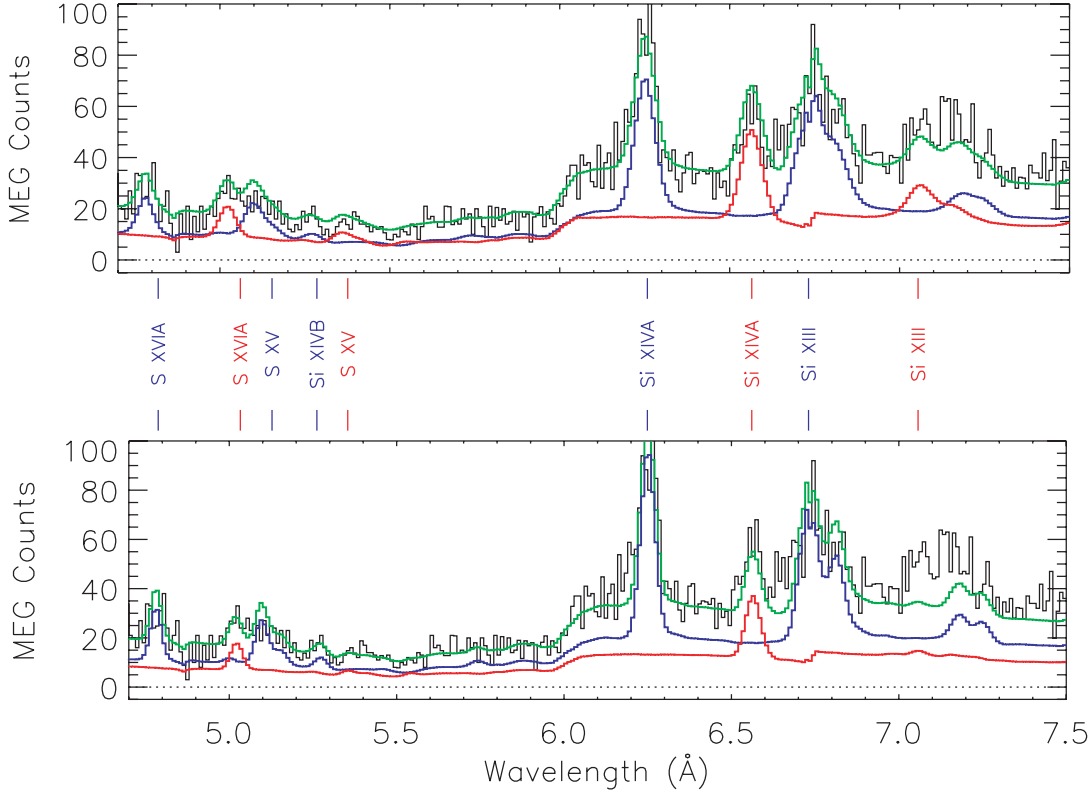
Fɪɢ. 8.—Same as Fig. 7, except plots with reasonable fits to the data. *Top:* Plot with the red jet zones 1 and 2 set to zero and with zone 3 at 70% of the zone 3 blue jet value. Although slightly above the data, the Si ɪᴠ and Si ɪɪɪ lines are reasonably predicted by the model. This result gives a lower limit on the temperature at which the companion blocks the red jet. *Bottom:* Plot using 60% of the second component normalization of the blue jet model while the third component normalization was set to zero. The model is a reasonable predictor for the observed lines (except around the Si fluorescence lines), and it places an upper limit on the temperature at which the companion blocks the red jet.

of the blue jet. Initially, the second- and third-component emission measures were set to zero, as displayed in Figure 7 (*bottom*). Then, the goodness of fit was tested for increasing values of the emission measures in zones 2 and 3 (for example, Fig. 7, *top*). Figure 8 displays the fits used to determine approximate confidence limits on T_x.

We define ζ as the ratio of the emission measures of the unocculted zones of the red and blue jets. If r_j is the distance from the apex of the cone to the center of zone j, then ζ is related to x_j, the distance from the origin of the red jet to the point of truncation (the truncation radius) in zone j, by

$$\zeta_j = \frac{\mathrm{EM}_{\mathrm{red},j}}{\mathrm{EM}_{\mathrm{blue},j}} = \frac{\int_{0.5r_j}^{x_j} n_e^2 \, dV}{\int_{0.5r_j}^{1.5r_j} n_e^2 \, dV} = \frac{3}{2}\left(1 - \frac{r_j}{2x_j}\right), \qquad (3)$$

using $n_e \propto r^{-2}$ and the definition of emission measure. Here $r_j = 1.83 \times 10^{11}$ cm for the second zone ($j = 2$), and $r_j = 9.19 \times 10^{10}$ cm for the third zone ($j = 3$) in the adiabatically cooled jet model from Paper I (see Table 3). Solving for x_j,

$$x_j = \frac{3r_j}{2}(3 - 2\zeta)^{-1}. \qquad (4)$$

By visual inspection, we identify a range of reasonable models for the data. Using this method, we obtain a lower limit emission measure of 5.4×10^{57} cm³ in the second zone and an upper limit of 1.16×10^{58} cm³ in the third zone. The lower and upper limits to the truncation radii using equation (4) are 5.1×10^{10} and 8.5×10^{10} cm, respectively. Thus, $x_j = (6.8 \pm 1.0) \times 10^{10}$ cm (1 σ uncertainties).

Other conditions (besides eclipse) might cause the dimming observed in the cool portion of the red jet. For example, an electron-scattering region could exist that linearly increases in optical depth with distance from the disk. Optical depth τ is related to jet length through the scattering region l by $\tau = \sigma_{\mathrm{T}} n_e l \geq 1$, where σ_{T} is the Thomson scattering cross section and n_e is the electron density. At the far side of the red jet, $l = 2r \cos \alpha$, where r is the jet length 2×10^{11} cm and $\alpha = 84°.6$ from § 3. Therefore,

$$n_e \geq \frac{1}{2\sigma_{\mathrm{T}} r \cos \alpha} \geq 3.6 \times 10^{13}\left(\frac{r}{2 \times 10^{11} \text{ cm}}\right)^{-1}. \qquad (5)$$

This electron density is comparable to that of the jet, so it seems unlikely that the jets propagate through such a thick medium. Similar difficulties arise when considering cold, neutral material. We approximate the path length through the medium to be 4×10^{10} cm. For intensity to drop by a factor of 2 for 2 keV photons, a column density of 2×10^{22} cm⁻² is necessary along this path length. Thus, the density of neutral material should be of the order of 5×10^{11} particles cm⁻³. This density is implausibly high, and we discount the possibility of either electron scattering by an ionizing gas or absorption by a cold, neutral gas.

5. DISCUSSION

5.1. *Examining the Adiabatic Expansion Model*

The thermal evolution of the jet depends on the relative dominance of two cooling terms: adiabatic expansion and radiative losses (Kotani et al. 1996). In the first HETGS observation, the emission measure distribution EM(T) was predicted adequately

from the adiabatic model. If adiabatic cooling dominates, then $T \propto r_j^{-4/3}$ for a nonrelativistic gas. Line profile measurements indicate that the jet is a conical, uniform velocity flow (see § 4), and $n_e n \propto r^{-4}$. Thus, $\mathrm{EM}(T) \propto r_j^{-1} \propto T^{3/4}$. The adiabatic model has shortcomings, as shown in Paper I. Examination of Table 3 reveals that the high-temperature point is too low and the zone 1 emission measure is too high. The high-temperature line emission could be reduced by Comptonization in the highest density portion of the jet. The disagreement in the lowest temperature zone may be attributed to statistical uncertainties of the order of 30% (consistent with Paper I) in detecting long-wavelength lines. Here we explore other possible effects influencing the emission measure.

The model fits require the abundances for metals that dominate the line emission (Fe, S, Si, Mg) to have changed from 1.3 times solar to 1.7 times solar between observations. If we assume a larger abundance, such as 2.0 times solar, and add a fifth spectral component, the continuum increases dramatically overall. In this model, the new component is thermal bremsstrahlung with sufficiently high temperature to strip detectable ions, $(3-5) \times 10^8$ K. At high energy, the component would turn over, consistent with early estimates of the peak temperature using *Ginga* (Brinkmann et al. 1991; Yuan et al. 1995). The plasma responsible for this X-ray emission, however, might originate from the disk corona rather than the jets.

Furthermore, the radiative cooling timescale is estimated to be substantially shorter than the flow time at the base of the jet. From Paper I, we expect a radiative cooling time $t_r \equiv kT/[\Lambda(T)n_e] \sim 0.3$ s, whereas the flow time is $t_a \equiv r_j/v_j = 2.8$ s. We will revisit the validity of the adiabatic model in a forthcoming paper (H. L. Marshall et al. 2006, in preparation). A model that may account for these dilemmas is one invoking substantially higher abundances. At the base of the jet where temperatures reach above 3×10^7 K, cooling is dominated by bremsstrahlung processes. Consequently, if the Si abundance is increased to ~ 10 times solar, the continuum is depressed ~ 10 times and the cooling rate drops by ~ 10 times. Thus, the cooling time would increase to ≈ 3 s. Coupled with a jet length decrease of $10^{1/3}$, the flow time t_a is below the radiative cooling time t_r after abundance effect considerations.

5.2. Fluorescence

We observed two unresolved, unshifted line complexes likely due to fluorescence: one at 1.942 ± 0.001 Å (Fe I–XII) and another at 7.131 ± 0.006 Å (Si I–V). The line fluxes are substantial, with 1.0×10^{-4} photons cm^{-2} s^{-1} for Fe and 1.4×10^{-5} photons cm^{-2} s^{-1} for Si, respectively. Adopting a distance of 4.85 kpc, the luminosities of these fluorescence lines are of the order of 10^{34} ergs s^{-1}. The stationary Fe I line emission was previously observed by Kotani et al. (1996) at comparable strength. They excluded the possibility of a large companion and, consequently, a substantial stellar wind, and they argued that the emission was likely due to partial illumination of an accretion disk by the central source. Given the moderate luminosity of the Fe I line, we suggest that this line emission originates near the companion, perhaps from clumps in a weakly ionized wind. Other high-mass X-ray binaries (HMXBs) such as Cyg X-1, Vela X-1, Cen X-3, and GX 301-2 have been observed to produce line fluxes orders of magnitude higher, except during eclipse (Nagase et al. 1994; Sako et al. 1999; Wojdowski et al. 2003). During occultation, the direct view of the compact object is obscured and the emission lines are attributed to dense material in the ionized winds rather than from the environment of the compact object. Likewise, the SS 433 fluorescence line luminosities are comparable to the
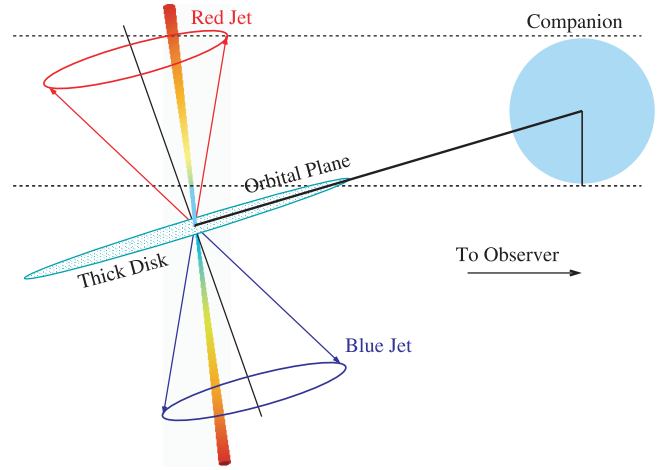

Fig. 9.—Schematic geometry of the system. During eclipse, the companion blocks the cool, outer portion of the red jet from the observer but not the hotter part that is closer to the compact object.

quiescent fluorescent line luminosity in 4U 1700−37 (Boroson et al. 2003). Consequently, the fluorescence line luminosities in SS 433 are similar to those of HMXBs during eclipse (Schulz et al. 2002; Boroson et al. 2003). The winds in these sources seem to have clumps of dense neutral and partially ionized material leading to fluorescence from Si I up to Si VIII ions (Schulz et al. 2002; Boroson et al. 2003). Si VII and VIII ions have higher yields than Si I ions. The absence of lines from these higher charge states indicates that the fluorescence in SS 433 originates from a much less ionized environment.

5.3. *Inferring the Binary Geometry and Black Hole Mass*

We assume that the system has the geometry shown in Figure 9 and approximate that the companion fully eclipses the receding jet for $r_j > x_j$. Our eclipse model requires that the disk be wind-fed and the companion star not fill its Roche lobe radius R_L, which is considered unlikely by some theorists (for example, King et al. 2000).

To examine this constraint of our model, we relate R_L to the semimajor axis a of the binary orbit and the mass ratio q of the central object to the companion star as described by Ritter (1988):

$$R_L = \frac{0.49 q^{-2/3} a}{0.6 q^{-2/3} + \ln(1 + q^{-1/3})}. \tag{6}$$

Using the geometry shown in Figure 10, the radius R of the companion is

$$R = (a - d)\cos i, \tag{7}$$

where d is the distance from the source of the jets to the point of intersection of the line of sight and the orbital plane and i is the angle of inclination. If the companion fills its Roche lobe radius, then $R_L = R$, and d can be expressed in terms of a, i, and q:

$$d = a \left[1 - \frac{0.49 q^{-2/3} \sec i}{0.6 q^{-2/3} + \ln(1 + q^{-1/3})} \right]. \tag{8}$$

With $i = 78°.83$ from the kinematic model (Margon & Anderson 1989), $d > 0$ implies $q > 13.5$. Reasonable values of q are in the range $0 < q < 1.5$, so our model requires that the companion star not fill its Roche lobe.
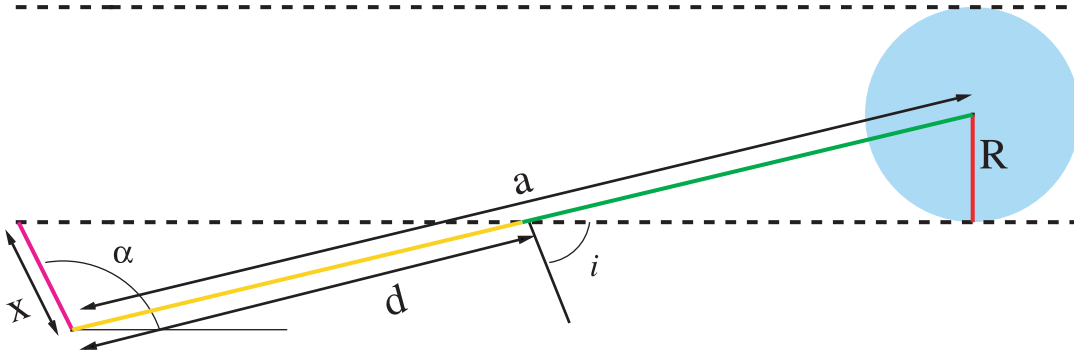
Fɪɢ. 10.—Geometry, as in Fig. 9, with distances and angles labeled. Appealing to basic trigonometry and geometry, we can use the measured value of *x* to find *R*, the radius of the companion. We calculate α in § 3, the system inclination *i* comes from the standard kinematic model (Margon & Anderson 1989), and the semimajor axis *a* is derived from the system mass ratio and the size of the companion's Roche lobe (which may not be filled; see § 5.3). Thus, by measuring the distance x_j using fits to the X-ray spectrum, we can determine the length *d* and the stellar radius, *R* (§ 5.3).

Using the angles intrinsic to the system in Figure 10, *d* can be calculated:

$$d = \frac{x_j \sin \alpha}{\sin (90 - i)}. \quad (9)$$

With x_j from § 4, $d = (3.5 \pm 0.8) \times 10^{11}$ cm. For a circular orbit, the semimajor axis *a* can be determined from the observable quantities K_x and K_o, the semiamplitude velocities of the compact object and companion, respectively:

$$a = \frac{P(K_x + K_o)}{2\pi \sin i} = \frac{PK_x(1 + q)}{2\pi \sin i}, \quad (10)$$

where $q \equiv M_x/M_o = K_o/K_x$, and M_x and M_o are the masses of the compact object and companion, respectively. With $K_x = 175 \pm 20$ km s^{-1} (Fabrika & Bychkova 1990) and $K_o = 100 \pm 15$ km s^{-1} (Gies et al. 2002a), $a = (3.8 \pm 0.4) \times 10^{12}$ cm.

Using equation (7), we find $R = (6.7 \pm 0.7) \times 10^{11}$ cm, or 9.6 ± 1.0 $R_\odot$. The uncertainty in the estimated radius is dominated by the uncertainty in the semimajor axis because *d* and its uncertainty are rather small compared to *a*. The value of *R* is approximately one-third of the Roche lobe radius of the companion. Therefore, if our model is correct, the companion does not fill the Roche lobe, and accretion probably occurs from a stellar wind, as might be expected from an early-type star. Given the small radius of the companion, we assume that it is a main-sequence star. Consequently, we can estimate its mass based on its radius.

From an empirical mass-radius relation for main-sequence stars (Demircan & Kahraman 1991), a radius of 9.6 ± 1.0 $R_\odot$ corresponds to a mass of 35 ± 7 $M_\odot$. A star this massive can have a very strong stellar wind, consistent with our model that the companion is smaller than the Roche lobe. Using K_x and K_o from above, we find that the mass of the compact object is 20 ± 5 $M_\odot$. This argument indicates that the compact object responsible for the relativistic jets is a black hole. We note that the validity of this result depends on the adequacy of the adiabatic model and the assumption that the red and blue jets have similar velocities and are co-axial. These issues will be explored in our subsequent paper on SS 433 (H. L. Marshall et al. 2006, in preparation).

In recent work, Hillwig et al. (2004) obtained different values for the mass ratio *q* (and consequently semimajor axis *a*) than the one used above. Based on weak absorption features in the optical spectra, they predict that the companion is an evolved A star with a mass $\approx 10.9 \pm 3.1$ $M_\odot$ and that the compact object is a black hole with mass $\approx 2.9 \pm 0.7$ $M_\odot$. This classification of the donor star is difficult because of the bright accretion disk that swamps signatures of the companion. Our model requires accretion to occur through a wind process, so the companion cannot be an A supergiant by our analysis. Future high-resolution optical and X-ray spectral observations of SS 433 are necessary to distinguish the true nature of the donor star.

To check the robustness in our determination of the companion's radius, we calculate *R* for different values of *q*. Gies et al. (2002b) estimate $q = 0.72$ and $a = 5.92 \times 10^{12}$ cm. Using equation (7), we find $R = 1.08 \times 10^{12}$ cm $= 15.50$ $R_\odot$ in this case. Hillwig et al. (2004) obtain $q = 0.26$ and $a = 3.08 \times 10^{12}$ cm, which corresponds to $R = 5.29 \times 10^{11}$ cm $= 7.60$ $R_\odot$. Values of $R \approx 7.6–15.5$ $R_\odot$ produce companion mass values between 25 and 80 $M_\odot$, and the resulting compact object mass is 6–60 $M_\odot$.

5.4. *Future Work*

This work generates numerous questions that we will address in upcoming papers. Foremost, our results rely on the assumptions that the adiabatic model adequately fits the observed X-ray spectra and that the jets have identical velocities and directions. As discussed in §§ 4 and 5.1, the adiabatic model has shortcomings, and we plan to reexamine the jet cooling using recent 200 ks HETGS observations of SS 433 (ObsIDs 5512, 5513, 5514, and 6360). In addition, the observed line broadening may arise from the divergence of conical outflow or from Doppler shift variations through the course of an observation (see § 3). We plan to constrain the origins of this broadening in our next paper as well. Further optical measurements are needed in order to determine K_o and K_x more definitively. These velocities are vital to firmly establish the nature of SS 433. We are currently completing simultaneous observations of SS 433 in the X-ray, optical, and radio bands in order to examine the jets and their changes as they move outward from the disk in a more comprehensive manner.

REFERENCES

Abell, G. O., & Margon, B. 1979, Nature, 279, 701
Begelman, M. C., Sarazin, C. L., Hatchett, S. P., McKee, C. F., & Arons, J. 1980, ApJ, 238, 722
Boroson, B., Vrtilek, S. D., Kallman, T., & Corcoran, M. 2003, ApJ, 592, 516
Brinkmann, W., Kawai, N., Matsuoka, M., & Fink, H. H. 1991, A&A, 241, 112
Canizares, C. R., et al. 2005, PASP, 117, 1144
Davidson, K., & McCray, R. 1980, ApJ, 241, 1082
Demircan, O., & Kahraman, G. 1991, Ap&SS, 181, 313
Fabian, A. C., & Rees, M. J. 1979, MNRAS, 187, 13P
Fabrika, S. N., & Bychkova, L. V. 1990, A&A, 240, L5
Fender, F., Migliari, S., & Méndez, M. 2003, NewA Rev., 47, 6
Gies, D. R., Huang, W., & McSwain, M. V. 2002a, ApJ, 578, L67
Gies, D. R., McSwain, M. V., Riddle, R. L., Wang, Z., Wiita, P. J., & Wingert, D. W. 2002b, ApJ, 566, 1069
Gladyshev, S. A., Goranskii, V. P., & Cherepashchuk, A. M. 1987, Soviet Astron., 31, 541
Hillwig, T. C., Gies, D. R., Huang, W., McSwain, M. V., Stark, M. A., van der Meer, A., & Kaper, L. 2004, ApJ, 615, 422
Hjellming, R., & Johnston, S. 1981, ApJ, 246, L141
King, A. R., Taam, R. E., & Begelman, M. C. 2000, ApJ, 530, L25
Kotani, T., Kawai, N., Matsuoka, M., & Brinkmann, W. 1996, PASJ, 48, 619
Kotani, T., et al. 1994, PASJ, 46, L147

Margon, B. 1984, ARA&A, 22, 507
Margon, B., & Anderson, S. F. 1989, ApJ, 347, 448
Margon, B., Ford, H. C., Katz, J. I., Kwitter, K. B., Ulrich, R. K., Stone, R. P. S., & Klemola, A. 1979, ApJ, 230, L41
Marshall, F. E., Swank, J. H., Boldt, E. A., Holt, S. S., & Serlemitsos, P. J. 1979, ApJ, 230, L145
Marshall, H. L., Canizares, C. R., Heinz, S., Hillwig, T. C., Mioduszewski, A. J., and Schulz, N. S. 2006, in Proc. Relativistic Astrophysics and Cosmology— Einstein's Legacy, ed. B. Aschenbach et al. (Berlin: Springer), in press
Marshall, H. L., Canizares, C. R., & Schulz, N. S. 2002, ApJ, 564, 941 (Paper I)
Milgrom, M. 1979, A&A, 76, L3
Nagase, F., Zylstra, G., Sonobe, T., Kotani, T., Inoue, H., & Woo, J. 1994, ApJ, 436, L1
Ritter, H. 1988, A&A, 202, 93
Sako, M., Liedahl, D., Kahn, S., & Paerels, F. 1999, ApJ, 525, 921
Schulz, N. S., Canizares, C. R., Lee, J. C., & Sako, M. 2002, ApJ, 564, L21
Stewart, G. C., et al. 1987, MNRAS, 228, 293
Vermeulen, R. C., Schilizzi, R. T., Spencer, R. E., Romney, J. D., & Fejes, I. 1993, A&A, 270, 177
Wojdowski, P. S., Liedahl, D. A., Sako, M., Kahn, S. M., & Paerels, F. 2003, ApJ, 582, 959
Yuan, W., Kawai, N., Brinkmann, W., & Matsuoka, M. 1995, A&A, 297, 451